ACS APPLIED MATERIALS & INTERFACES

Research Article

Cite This: *ACS Appl. Mater. Interfaces* XXXX, XXX, XXX−XXX

www.acsami.org

Thermal and Plasma-Enhanced Atomic Layer Deposition of Yttrium Oxide Films and the Properties of Water Wettability

Bo Zhao, Felix Mattelaer, Geert Rampelberg, Jolien Dendooven, and Christophe Detavernier*

Department of Solid State Sciences, Ghent University, Krijgslaan 281 S12, 9000 Ghent, Belgium

Supporting Information

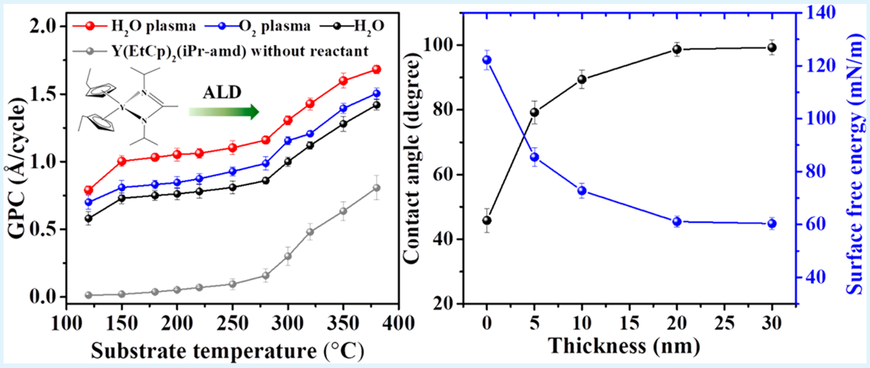

ABSTRACT: The atomic layer deposition (ALD) of yttrium oxide (Y_2O_3) is investigated using the liquid precursor Y(EtCp)$_2$(iPr-amd) as the yttrium source with thermal (H_2O) and plasma-enhanced (H_2O plasma and O_2 plasma) processes, respectively. Saturation is confirmed for the growth of the Y_2O_3 films with each investigated reactant with a similar ALD window from 150 to 300 °C, albeit with a different growth rate. All of the as-deposited Y_2O_3 films are pure and smooth and have a polycrystalline cubic structure. The as-deposited Y_2O_3 films are hydrophobic with water contact angles >90°. The water contact angle gradually increased and the surface free energy gradually decreased as the film thickness increased, reaching a saturated value at a Y_2O_3 film thickness of ~20 nm. The hydrophobicity was retained during post-ALD annealed at 500 °C in static air for 2 h. Exposure to polar and nonpolar solvents influences the Y_2O_3 water contact angle. The reported ALD process for Y_2O_3 films may find potential applications in the field of hydrophobic coatings.

KEYWORDS: *atomic layer deposition, plasma-enhanced, heteroleptic precursor, yttrium oxide, water contact angle*

1. INTRODUCTION

Yttrium oxide (Y_2O_3) offers material properties that are attractive to specific applications. Its high refractive index of 1.9 is useful for the fabrication of planar waveguides in solid-state and high-power lasers.[1] Bulk Y_2O_3 has a high thermal conductivity of 0.27 W (cm K)$^{-1}$ at 300 K, a high melting point of 2430 °C, and a high mechanical strength, which makes it an interesting material for temperature- and wear-resistant coatings.[2−5] Y_2O_3 has numerous applications in the fields of electronics and optoelectronics.[6−9] For example, thin films of Y_2O_3 are suited as high-*k* gate dielectrics due to the large intrinsic band gap in the range of 5.5 to 5.8 eV and the high dielectric constant of 14−18. For this reason, Y_2O_3 thin films are intensively studied in metal oxide semiconductor field effect transistors (MOSFETs) as the thin high-*k* gate material.[10] Moreover, Y_2O_3 thin films have been employed as optical and protective coatings, buffer layers in ferroelectrics and superconductors, as well as dielectric insulators in electroluminescent devices.[11−14] For example, the rare-earth-doped Y_2O_3 films, such as Eu:Y_2O_3,[15,16] Er:Y_2O_3,[17] Er:Eu:Y_2O_3,[18] and Er:Yb:Y_2O_3,[19] have been widely used in photonic devices, like optical amplifiers, sensors, up-converters, light-emitting diodes (LEDs), organic LEDs, and thin-film electroluminescent devices. In addition, Y_2O_3-based films, such as yttria-stabilized zirconia (YSZ) and yttria-doped ceria (YDC), are applied as solid-state electrolytes for solid oxide fuel cells (SOFCs).[20−25]

There have been a variety of methods used to deposit thin films of Y_2O_3, including physical vapor deposition (PVD),[26] chemical vapor deposition (CVD),[27] plasma-enhanced chemical vapor deposition (PECVD),[28] and atomic layer deposition (ALD). Studies such as these have shown that important film properties such as crystallinity, residual carbon content, and electronic properties are influenced by the choice of deposition method as well as the particular precursor/reactant used. Among them, ALD has attracted much interest because it is able to produce high-quality, uniform, and conformal films with excellent composition and submonolayer thickness control, even at low growth temperatures based on self-limited surface reactions.[29−31] During ALD, the film grows through

Received: October 10, 2019
Accepted: December 20, 2019
Published: December 20, 2019

DOI: 10.1021/acsami.9b18412

the surface reactions of vaporized precursors and reactant gases that are alternately supplied to the substrate surface. The choice of the proper metal precursor is crucial for a successful ALD process. The main requirements for ALD precursors concern a suitable vapor pressure at its supplying temperature, no self-decomposition at the process temperature, and an aggressive reaction with surface groups.[32,33]

In prior research on the ALD of Y_2O_3, thermal or plasma-enhanced techniques with various types of precursors have been explored, as summarized in Table 2. Cyclopentadienyl-(Cp-) based precursors, $Y(Cp)_3$,[34] $Y(MeCp)_3$,[35] $Y(EtCp)_3$,[36] and $Y(iPrCp)_3$,[37] are solid at room temperature (RT) and show high growth rates and reactivity toward water, O_2 plasma, or O_3 but suffer from poor thermal stability. O-coordinated β-diketonate $Y(thd)_3$[38] is solid at RT and offers good thermal stability but requires sublimation over 130 °C while exhibiting a growth rate of only 0.23 Å per cycle at a high substrate temperature of 350 °C, and the deposited film was reported to contain carbon 1.4% impurities. To reduce the carbon level in the films, N-coordination and heteroleptic precursors have been evaluated, like $Y(DPDMG)_3$,[39] $Y(iPr_2\text{-amd})_3$,[40] and $Y(iPrCp)_2(iPr\text{-amd})$.[41−43] $Y(DPDMG)_3$ is solid at RT and requires sublimation over 130 °C, and the deposited film was reported to contain 3 at % N and 2 at % C impurities. $Y(iPr_2\text{-amd})_3$ is solid at RT, and growth resulted in a film with a high O content (Y/O ratio of 0.5). Whereas solid precursors may have similar thermodynamic vapor pressures with liquid precursors, they are still limited by the slower kinetics of vaporization. Therefore, liquid precursors are preferred for ALD processes. The heteroleptic $Y(iPrCp)_2(iPr\text{-amd})$, which consists of cyclopentadienyl and amidinate ligands, is the only liquid precursor reported so far in the literature. The $Y(EtCp)_2(iPr\text{-amd})$ discussed in this work is also liquid at RT and will be shown to enable a significantly higher growth rate compared with $Y(iPrCp)_2(iPr\text{-amd})$.

Hydrophobic coatings are widely used in applications ranging from industrial components to housewares.[44,45] Inorganic metal oxide hydrophobic coatings have attracted more and more interest because of the better mechanical durability and thermal stability than traditional polymer hydrophobic coatings.[46] ZnO[47,48] and TiO_2[49,50] are the most researched, but the hydrophobicity was not retained after either high-temperature annealing or UV exposure. Recently, rare-earth oxides were studied as hydrophobic materials. Varanasi et al.[51] and Kim et al.[52] reported that Er_2O_3, Dy_2O_3, La_2O_3, Y_2O_3, CeO_2, Pr_6O_{11}, Nd_2O_3, Sm_2O_3, Eu_2O_3, Gd_2O_3, Tb_4O_7, Ho_2O_3, Tm_2O_3, Yb_2O_3, and Lu_2O_3 films show high hydrophobicity with water contact angles >90°. Therefore, it can be concluded that rare-earth oxides have potential applicability as robust hydrophobic surfaces.

In this work, we report the ALD of Y_2O_3 films from a liquid heteroleptic precursor, yttrium bis-ethylcyclopentadienyl-diisopropylacetamidinate, $Y(EtCp)_2(iPr\text{-amd})$, for which the chemical structure is shown in Figure 1, with thermal (H_2O) and plasma-enhanced (H_2O plasma and O_2 plasma) processes, respectively. The ALD process conditions that are required to deposit Y_2O_3 films are investigated and optimized. The morphology, conformality, crystallinity, and composition of the grown films are characterized. Finally, we investigated the water wettability of Y_2O_3 films and the influence of exposure to different solvents (hexane, toluene, ethanol and isopropanol) on their wetting properties.

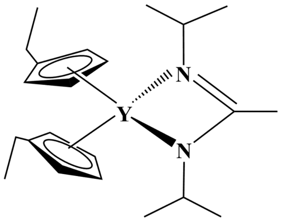

Figure 1. Chemical structure of the $Y(EtCp)_2(iPr\text{-amd})$ precursor.

2. EXPERIMENTAL SECTION

2.1. ALD of Y_2O_3 Thin Films. The Y_2O_3 films were grown on Si (100) substrates with a native oxide layer in a home-built high-vacuum ALD system with a base pressure $<5 \times 10^{-6}$ mbar.[53−55] In the ALD process, $Y(EtCp)_2(iPr\text{-amd})$ (supplied by AirLiquide) was used as the Y source. As reactant gases, water, oxygen plasma, and water plasma were tested, respectively. The oxygen and water plasma pulses of 1×10^{-2} mbar were performed with a radio frequency remote plasma source of 13.56 MHz and a power of 200 W. The ALD chamber and walls were heated to 100 °C. The $Y(EtCp)_2(iPr\text{-amd})$ precursor was held in a stainless-steel container at 120 °C for optimal vapor pressure without decomposition, and the delivery line was maintained at 130 °C to avoid precursor condensation. Argon was used as the carrier gas for $Y(EtCp)_2(iPr\text{-amd})$ precursor delivery to the ALD chamber. Water was kept at room temperature, and the delivery line was heated to 50 °C.

2.2. Characterization of Y_2O_3 Thin Films. X-ray reflectometry (XRR) and X-ray diffraction (XRD) patterns were acquired on Bruker D8 diffractometers using Cu Kα radiation (λ = 0.154 nm). The film thickness and density were determined from XRR by fitting simulated patterns to the measured ones. In situ spectroscopic ellipsometry (SE) measurements were performed with a J. A. Woollam M-2000 ellipsometer with a wavelength from 245 to 1000 nm and using the CompleteEASE software for fitting and data analysis. Surface morphology was characterized by scanning electron microscopy (SEM, Quanta 200F FEI) and atomic force microscopy (AFM) in tapping mode by using a Bruker Dimension Edge system. X-ray photoelectron spectroscopy (XPS) analysis was performed on a Thermo Scientific Theta Probe XPS instrument using Al Kα (λ = 0.834 nm) X-rays generated at 15 kV and 70 W and focused to a spot size of 0.3 mm by an MXR1 monochromator gun. The sample surface was etched by Ar^+ ions at an acceleration voltage of 3 keV and a current of 2 μA. After the measurements, the resulting spectra were analyzed with the CasaXPS software package for the calculation of atomic concentrations. Fourier transform infrared spectroscopy (FT-IR, Vertex V70 Bruker) was used to detect surface chemical functional groups. The data were collected from 600 to 4000 cm^{-1} with a resolution of 4 cm^{-1}.

2.3. Water Contact-Angle Measurements. The water wettability of ALD Y_2O_3 films was evaluated by the sessile drop technique using a contact-angle analyzer (Kruss, DSA30) with deionized water. Contact-angle images were acquired by a charge-coupled device video camera and Drop Shape Analysis software. The volume of each deionized water droplet used was 4 μL. For the thermal stability experiments, ALD Y_2O_3 films were annealed in a furnace at 500 °C for 2 h in the static air, after which the contact angle was measured. We used a dipping method to simulate the effect of different ambient conditions on the water wettability of Y_2O_3 films.[56] Hexane, toluene, ethanol, and isopropanol were investigated as the dipping solvents, respectively. A 2 cm × 2 cm piece of Si wafer was immersed in the solvent for 24 h, taken out, and left to dry in the air naturally, after which we measured the water contact angle. All of the contact-angle values in this work are reported as the average value recorded by the analyzer system.

3. RESULTS AND DISCUSSION

3.1. ALD of Y_2O_3 with Thermal (H_2O) and Plasma-Enhanced (O_2 Plasma and H_2O Plasma) Process. In a true

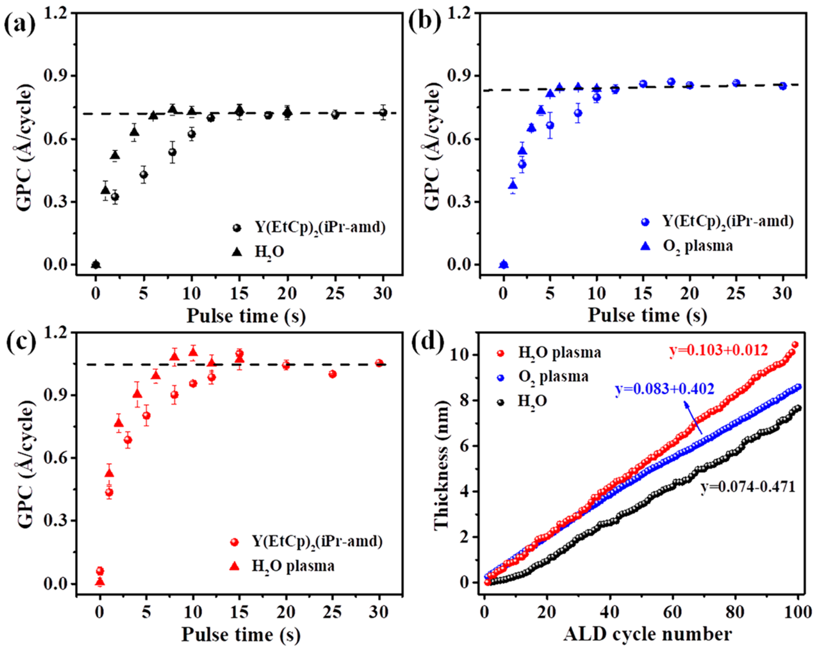

Figure 2. Saturation plots of ALD Y_2O_3 films at a substrate temperature 200 °C with $Y(EtCp)_2$(iPr-amd) and (a) H_2O, (b) O_2 plasma, and (c) H_2O plasma as a reactant. (d) Film thickness determined by in situ SE versus the ALD cycle number under saturated conditions.

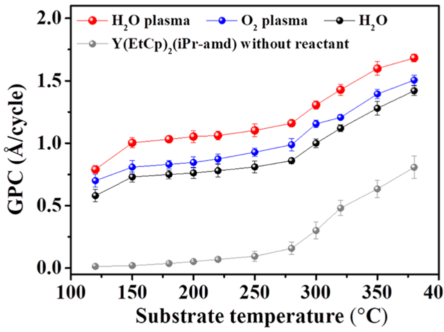

Figure 3. GPC as a function of substrate temperature.

ALD process, the precursor surface reactions must be self-terminating and complementary to yield a uniform, conformal, and high-quality Y_2O_3 thin film. To verify that the surface reaction for $Y(EtCp)_2$(iPr-amd) is really self-terminating, the effects of pulse time and substrate temperature were investigated. Figure 2a shows the results by monitoring the growth per cycle (GPC) as a function of both $Y(EtCp)_2$(iPr-amd) and H_2O pulse times at a constant temperature of 200 °C. The GPC for $Y(EtCp)_2$(iPr-amd) is saturated when the pulse time exceeds 15 s. This result indicates that $Y(EtCp)_2$(iPr-amd) undergoes a self-terminating reaction with the Y_2O_3 surface prepared by the reaction with H_2O. The H_2O pulse time is saturated when it exceeds at 10 s. This suggests that H_2O undergoes a self-terminating reaction with surface-absorbed $Y(EtCp)_2$(iPr-amd) molecules. The saturated GPC is 0.74 Å/cycle. The plasma-enhanced process includes O_2 plasma and H_2O plasma, showing similar behaviors characteristic of a saturated reaction. For the O_2 plasma case, saturation was achieved after $Y(EtCp)_2$(iPr-amd) 12 s/O_2 plasma 8 s and yielded a slightly higher GPC of 0.83 Å/cycle (Figure 2b). For H_2O plasma, saturation was achieved at a 1.03 Å/cycle of $Y(EtCp)_2$(iPr-amd) 15 s/H_2O plasma 8s (Figure 2c). To understand the deposition kinetics, the thickness was monitored as a function of the cycle number under the saturation conditions of $Y(EtCp)_2$(iPr-amd) and the reactant at a constant temperature of 200 °C (Figure 2d). For the water thermal process, growth inhibition of ~15 cycles could be observed, but after ~15 cycles, the film thickness increased linearly as a function of the number of ALD cycles. The slope of the linear line is the GPC value, which corresponds to the GPC of the saturation time test (Figure 2a). For the plasma process (O_2 plasma and H_2O plasma), no growth inhibition was observed, and the slopes were also consistent with the GPC mentioned under the saturated conditions (Figure 2b,c).

As shown in Figure 3, all three reactants (H_2O, O_2 plasma, and H_2O plasma) have the same type of temperature window, with a nearly constant GPC value between 150 and 300 °C. In addition, there is almost no growth when only $Y(EtCp)_2$(iPr-amd) pulses without any reactant (gray dots), which indicates that the $Y(EtCp)_2$(iPr-amd) precursor is stable and does not decompose between 150 and 300 °C. Below 150 °C, the GPC decreases slightly, whereas above 300 °C the GPC increases abruptly with increasing substrate temperature. This suggests that the $Y(EtCp)_2$(iPr-amd) precursor molecules are chemisorbed with self-saturation on the surface at 150−300 °C, whereas an incomplete reaction occurs below 150 °C, and accelerated decomposition occurs above 300 °C. So in the mention of this work, we performed deposition at a substrate temperature of 200 °C.

Figure 4 shows the representative AFM images and corresponding XRR patterns. The resulting films were acquired after 250 ALD cycles of $Y(EtCp)_2$(iPr-amd) with H_2O, O_2 plasma, and H_2O plasma, respectively. For the AFM images, the scanned area is 3 × 3 μm^2. The surface morphology appears homogeneous and exhibits relatively low root-mean-square (RMS) roughness of ~0.41 nm with H_2O (Figure 4a), ~0.73 nm with O_2 plasma (Figure 4b), and ~0.64 nm with H_2O plasma (Figure 4c). From XRR and fitting results (Figure 4d), the density of the film is 4.88 g/cm^3 with H_2O as reactant,

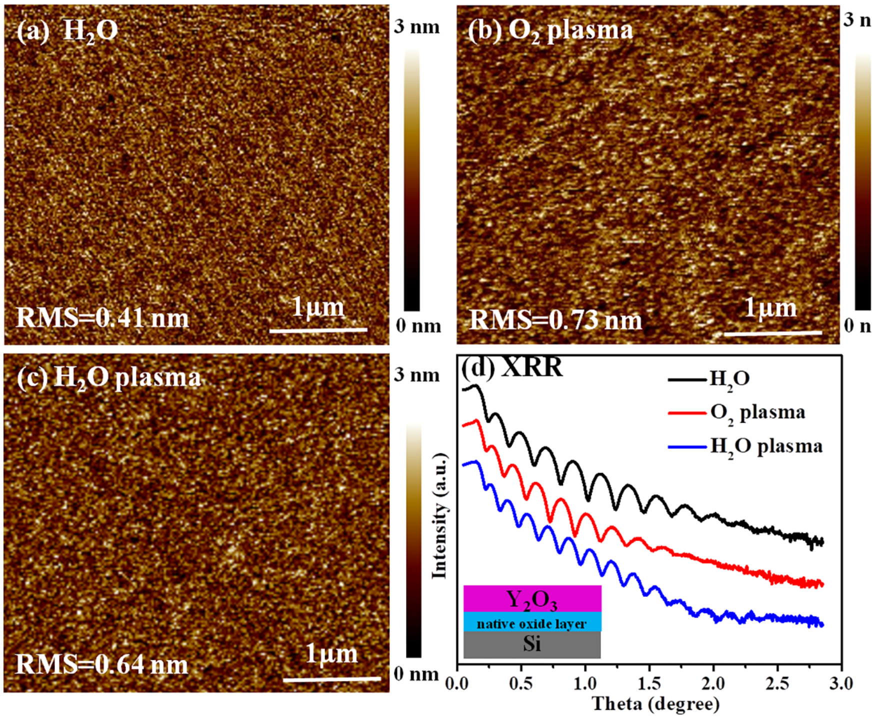

Figure 4. AFM images of Y_2O_3 films for $Y(EtCp)_2(iPr\text{-}amd)$ with (a) H_2O, (b) O_2 plasma, and (c) H_2O plasma and (d) the corresponding XRR patterns.

Table 1. Thickness, Density, and Roughness of Y_2O_3 Films after 250 ALD Cycles[a]

ALD reactant	thickness determined by in situ SE (nm)	thickness determined by XRR (nm)	density determined by XRR(g/cm^3)	roughness determined by XRR (nm)	roughness determined by AFM (nm)
H_2O	18.5	19.4	4.88	0.43	0.41
O_2 plasma	21.0	21.6	4.97	0.95	0.73
H_2O plasma	25.7	24.7	4.92	0.82	0.64

[a] Results are from measurements of SE, XRR, and AFM.

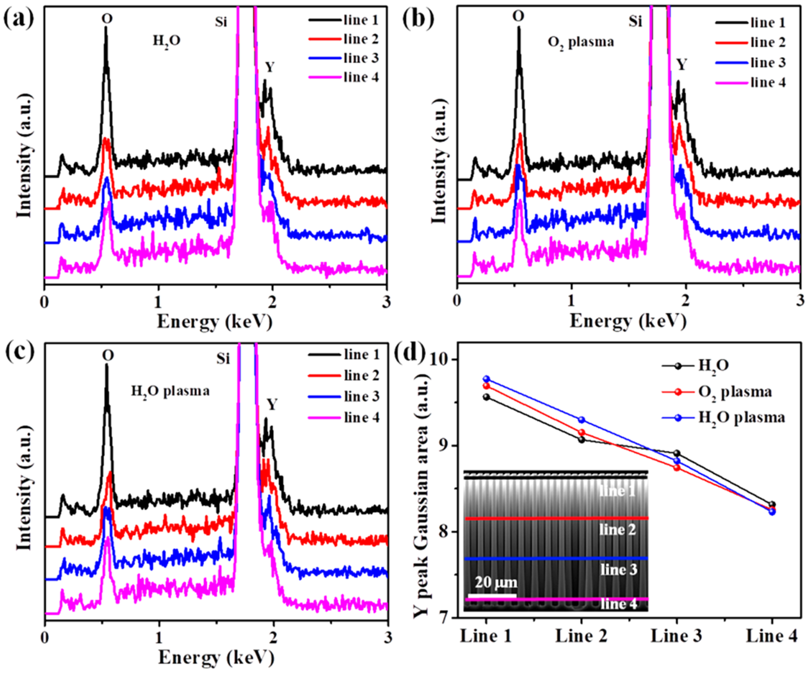

Figure 5. EDX spectra of the Y_2O_3 coating layer at four different positions in silicon micropillar arrays (panel d inset) of (a) with H_2O, (b) O_2 plasma, and (c) H_2O plasma. (d) Y peak Gaussian area at four different depths acquired from EDX line scans.

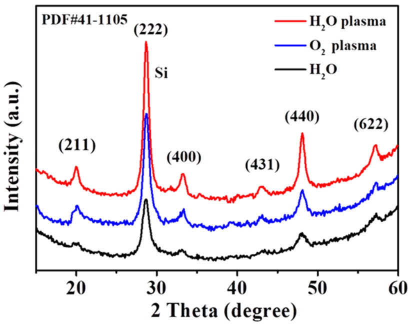

Figure 6. XRD patterns of Y_2O_3 films for $Y(EtCp)_2(iPr\text{-}amd)$ with H_2O, O_2 plasma, and H_2O plasma.

4.97 g/cm^3 with O_2 plasma, and 4.92 g/cm^3 with H_2O plasma. These values are lower than the value of 5.03 g/cm^3 reported for the bulk density of Y_2O_3, which is probably related to the inclusion of −OH. The densities for the plasma-enhanced processes (O_2 plasma and H_2O plasma) are slightly higher than that of the thermal process. The thickness determined by XRR is similar to the results of SE, indicating that the Cauchy model used for analyzing the in situ SE data is indeed suitable. The roughness determined by XRR is also close to the results of AFM. All results are summarized in Table 1.

Conformality is an important aspect of ALD process development, as it is the ability to conformally deposit a film on a substrate, especially for the 3D complex structures with ideally no variation in thickness along with the structure.[29,30] Here the conformality of the coating was investigated by depositing a 10 nm Y_2O_3 film with H_2O, O_2 plasma, and H_2O plasma, respectively, on a high-aspect-ratio (AR) structure consisting of silicon micropillars with an AR of 25 (namely, 2 μm wide, 50 μm high, spaced 4 μm center-to-center on a square lattice) etched into a silicon substrate, shown in Figure 5. The as-deposited samples were measured with SEM and energy-dispersive X-ray spectroscopy (EDX) to evaluate the amounts of yttrium at different depths (Figure 5d, inset). The EDX spectra in Figure 5a show the Y_2O_3 coating from $Y(EtCp)_2(iPr\text{-}amd)$ with H_2O and clearly demonstrate the Y peak, indicating the presence of Y_2O_3. For the O_2 plasma (Figure 5b) and H_2O plasma (Figure 5c), the samples show the same trend from top to bottom on the micropillars. To distinguish the Si and Y signals, we fitted the EDX spectra with a Gaussian equation (see the Supporting Information) to get the Y peak area as a function of depth along the pillars. At the second marker on the cross-sectional SEM image (line 2), which is 17 μm deep along the pillars, the peak area of Y maintained ~94% of the initial value on line 1, and even at the bottom of the pillars, the Y peak area is still >85% of its initial value (Figure 5d). These results indicated that for the thermal (H_2O) and plasma-enhanced (O_2 plasma and H_2O plasma) processes, the pillars are fully coated with a reasonable conformality, although the amounts are not perfectly constant as a function of the penetration depth.

The crystalline structure of 30 nm Y_2O_3 films on Si substrates was determined by XRD. All three investigated reactants yield polycrystalline cubic Y_2O_3 (JCPDS 41-1105).[38] The corresponding lattice planes are labeled for the different diffractions peaks in Figure 6. It demonstrates that the normal direction of the (222) plane is the most obvious, whereas the (211), (400), (431), (440), and (622) planes of cubic Y_2O_3 are also clearly observed.

The chemical binding environments in as-deposited Y_2O_3 films were studied by XPS, and the results are shown in Figure 7. All of the data were collected after Ar^+ beam sputtering 20 s from the surface to remove carbon surface contaminants. Figure 7a shows that all of the films deposited using different processes contain Y and O, whereas no N is detected, suggesting that the N-coordination from the $Y(EtCp)_2(iPr\text{-}amd)$ molecule was not retained in the film. After sputtering, no C contamination in the bulk of the films could be detected. As shown in the Y 3d core-level spectrum of the as-deposited films (Figure 7b), the peak at 157.6 eV can be assigned to Y $3d_{5/2}$, and the shoulder peak at 159.6 eV is identified as Y $3d_{3/2}$. In Figure 7c, the peaks assigned to O 1s for the three reactants have some slight variations around 530.1 eV, possibly due to the different contents of Y−O and Y−OH.[57] The impurity content of C is <0.5 at %, and the atomic ratio of Y/O is 0.57 to 0.60 for the Y_2O_3 films by the three processes, indicating the deposition of a high-purity Y_2O_3 film.

From the above characterizations, we know that the as-deposited Y_2O_3 films are pure (with C and N impurity levels below 0.5 at %) and smooth and have a polycrystalline cubic structure. To make a comprehensive assessment of our results, we summarized existing literature on the ALD of Y_2O_3 using different precursors in Table 2. The $Y(EtCp)_2(iPr\text{-}amd)$ used in this research and $Y(iPrCp)_2(iPr\text{-}amd)$ are the only liquid precursors reported so far. When compared with $Y(iPrCp)_2(iPr\text{-}amd)$, the $Y(EtCp)_2(iPr\text{-}amd)$ explored in this work was demonstrated to offer a significantly higher growth rate as well as a wider temperature window. All other precursors listed in Table 2 are solids, require a high source temperature, and suffer from a low GPC or from C/N impurities in the deposited films.

3.2. Water Wettability of Y_2O_3 Films.

Figure 8 shows the measured water contact angle values as a function of the Y_2O_3 film thickness varying from 5 to 30 nm for the investigated three different ALD processes. The water contact angle of the Si substrate with a native oxide layer is ~40° without ALD

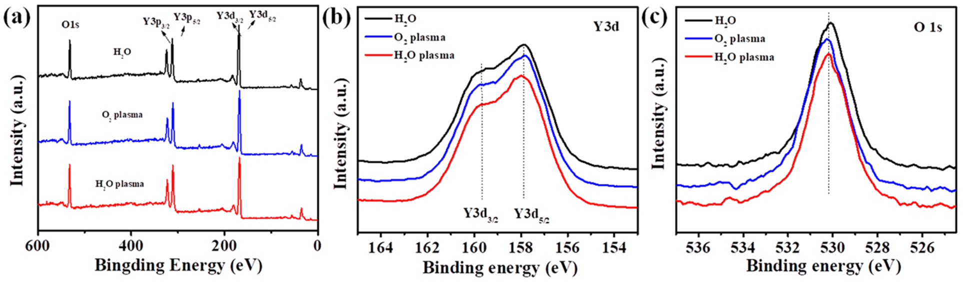

Figure 7. XPS spectra of Y_2O_3 films of (a) survey, (b) Y 3d, and (c) O 1s for $Y(EtCp)_2(iPr\text{-}amd)$ with H_2O, O_2 plasma, and H_2O plasma.

Table 2. ALD of Y_2O_3 Using Different Precursors and Relevant Process and Film Properties

precursor + reactant		precursor state at RT	bubbler temp (°C)	substrate temp (°C)	GPC (Å/cycle)	impurity (at %)	Y/O (at)	ref
$Y(Cp)_3 + H_2O$		solid	150	250−400	1.5−1.7	C 0.5, 300 °C	∼0.68, 300 °C	34
$Y(MeCp)_3 + O_2$ plasma		solid	145	175−325	1.1−1.3	C 0.85, 300 °C	not reported	35
$Y(EtCp)_3 + H_2O$		solid	120	250−280	1.5−1.7	C < 0.5, 250 °C	∼0.64, 250 °C	36
$Y(iPrCp)_3 + O_3$		solid	130	245−300	1.6−1.8	C < 0.5, 270 °C	∼0.29, 270 °C	37
$Y(thd)_3 + O_3$		solid	120	250−350	0.23	C 1.0−1.4, 350 °C	∼0.62, 350 °C	38
$Y(DPDMG)_3$		solid	130	175−250	1.1	C, 2; N 3, 225 °C	∼0.5, 225 °C	39
$Y(iPr_2\text{-amd})_3 + H_2O$		solid	120	150−280	0.8	C, N <0.5, 280 °C	∼0.5, 280 °C	40
$(iPrCp)_2Y(iPr\text{-amd}) + H_2O^a$		liquid	150	350−450	0.6	C, N <0.5, 350 °C	∼0.62, 350 °C	41
$Y(^iPrCp)_2\ (^iPr\text{-amd})^a$	$+ H_2O$	liquid	130	200−350	1.3	C 3.7 ± 0.4, 300 °C	∼0.56, 300 °C	42
	O_3					C 5.6 ± 0.5, 300 °C	∼0.48, 300 °C	
$Y(iPrCp)_2(N\text{-}iPr\text{-amd}) + H_2O^a$		liquid	130	180−200	0.4	C, N ∼0.1, 180 °C	not reported	43
$Y(EtCp)_2$ (iPr-amd)	$+ H_2O$	liquid	120	150−300	0.74	C, N <0.5, 200 °C	∼0.57, 200 °C	this work
	O_2 plasma				0.83	C, N <0.5, 200 °C	∼0.60, 200 °C	
	H_2O plasma				1.03	C, N <0.5, 200 °C	∼0.58, 200 °C	

[a] $Y(iPrCp)_2(N\text{-}iPr\text{-amd})$, $(iPrCp)_2Y(iPr\text{-amd})$, and $Y(^iPrCp)_2(^iPr\text{-amd})$ have the same chemical structure.

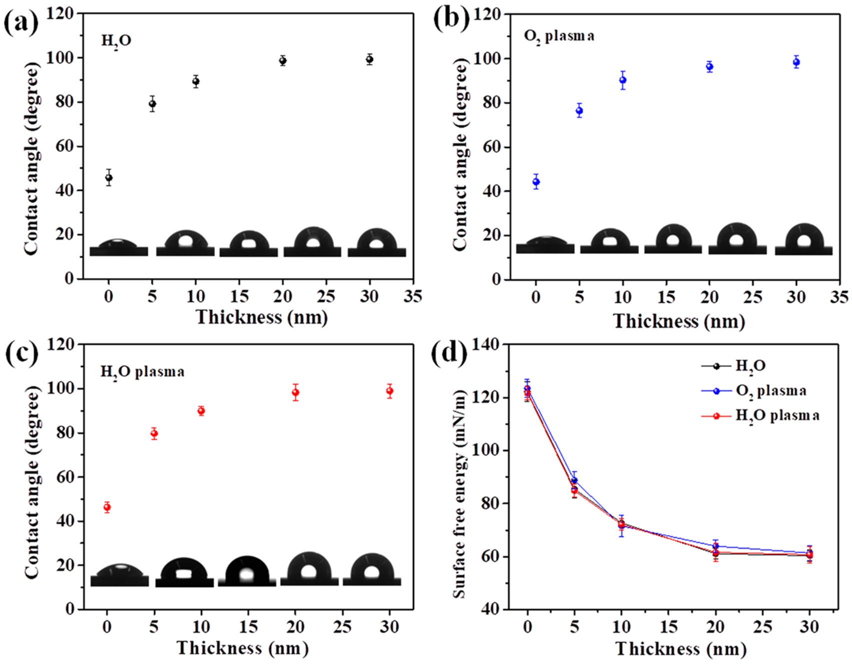

Figure 8. Water contact angles of as-deposited and Y_2O_3 films with a thickness of 5, 10, 20, and 30 nm with (a) H_2O, (b) O_2 plasma, (c) H_2O plasma, and (d) the surface free energy.

growth of Y_2O_3, showing the typically hydrophilic property. For the Y(EtCp)2(iPr-amd) with H_2O process (Figure 8a), the 20 and 30 nm Y_2O_3 films yielded a water contact angle of ∼95°. The water contact angle reduced to 87° for 10 nm Y_2O_3 ALD films and even to 77° for 5 nm films. A similar thickness dependency was also observed for the other two reactants, O_2 plasma (Figure 8b) and H_2O plasma (Figure 8c). Figure 8d shows the surface free energy calculated from the water contact angle of ALD Y_2O_3 films with different thicknesses by the Young−Dupré equation[58]

$$W = \gamma(1 + \cos\theta)$$

where W is the surface free energy (N/m), γ is the surface tension of water, which is a constant of 0.072 J/m^2, and θ is the water contact angle. The three reactants show similar results. An inverse relationship between water contact angle values and the surface free energy is observed with increasing the thickness of Y_2O_3. The thinner the film, the smaller the water contact angle and the higher the surface free energy, which is more easily wetted with water. All of the investigated films with a thickness >20 nm have a stable water contact angle

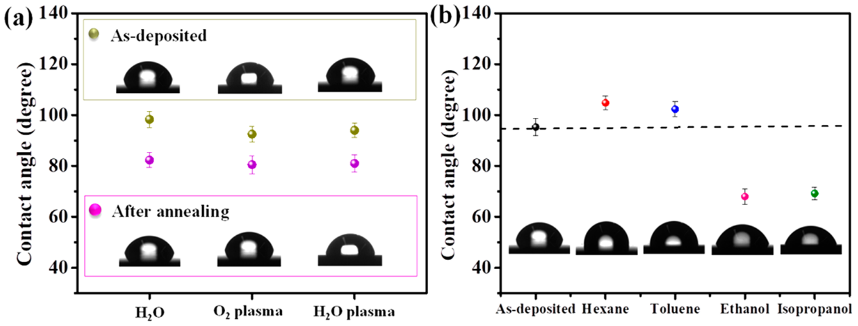

Figure 9. Water contact angles of as-deposited 30 nm thick Y_2O_3 surfaces (a) before and after annealing at 500 °C for 2 h in static air and (b) after treatment with hexane, toluene, ethanol, and isopropanol for 24 h.

of ~95°, which indicates that they are with a hydrophobic surface. To obtain a stable water contact angle, the work described later about the water wettability was performed using 30 nm films.

To evaluate the effect of ALD post-annealing on the wettability of the Y_2O_3 surfaces, we annealed the ALD Y_2O_3 films at 500 °C for 2 h in static air. As shown in Figure 9a, the water contact angles of annealed ALD Y_2O_3 films were slightly smaller than those of as-deposited samples but still maintained values around 80°, which indicates the quite robust behavior of the surfaces wettabilities.[59] The exact nature and composition of the surface are important factors for the material's water wettability. Adsorbed molecules can have a significant impact on the water contact angle.[60−63] Therefore, we investigated the influence of four different solvents (hexane, toluene, ethanol, and isopropanol) on the water contact angle of Y_2O_3 films. After immersing Y_2O_3 ALD films in these solvents for 24 h, the water wettability was evaluated. Figure 9b demonstrates that exposure of the Y_2O_3 surface to typical nonpolar solvents like hexane and toluene enhanced the hydrophobicity, as the water contact angle increased to 104.8 and 102.3°, respectively, which is higher than the value of 95° measured for the as-deposited Y_2O_3. Exposure to polar solvents like ethanol and isopropanol induced a hydrophilic effect, decreasing the water contact angle to 68 and 69.2°, respectively. The FT-IR data of as-deposited Y_2O_3 and after exposure to hexane, toluene, ethanol, and isopropanol are shown in Figure S3.

4. CONCLUSIONS

We have successfully fabricated ALD−Y_2O_3 films using a liquid heteroleptic Y precursor, $Y(EtCp)_2(iPr\text{-}amd)$, and investigated H_2O, O_2 plasma, and H_2O plasma as reactants, respectively. The growth of the Y_2O_3 films with each investigated reactant can get saturated with a similar ALD window from 150 to 300 °C but with a different growth rate. All of the as-deposited Y_2O_3 films are pure and smooth and have a polycrystalline cubic structure. Compared with other Y precursors, $Y(EtCp)_2(iPr\text{-}amd)$ is a liquid, requires a lower source temperature (~120 °C), offers a wide temperature window for ALD (150 to 300 °C), and enables the deposition of high-purity films (C/N impurities below 0.5 at %) at a high growth rate (0.74 to 1.03 Å/cycle), which renders it a promising precursor for industrial applications. The as-deposited Y_2O_3 films are hydrophobic with a water contact angle of ~95°. The hydrophobicity was retained during post-ALD annealing and could be altered by exposure to various solvents.

■ ASSOCIATED CONTENT

Ⓢ Supporting Information

The Supporting Information is available free of charge at https://pubs.acs.org/doi/10.1021/acsami.9b18412.

> Figure S1. SEM image of 3D pillars coated with the $Y(EtCp)_2(iPr\text{-}amd)$ and H_2O process and the EDX spectra for line scans as indicated on the SEM image. Figure S2. Gaussian fit spectra in Figure S1. Table S1. Y Gaussian peak area corresponding to the position of the Figure S1 SEM image. Table S2. Y peak area corresponding to the different depths on the cross-sectional SEM image for the $Y(EtCp)_2(iPr\text{-}amd)$ O_2 plasma and H_2O plasma process. Figure S3. FT-IR spectra of a 30 nm thick Y_2O_3 film, as-deposited and after exposure to hexane, toluene, ethanol, and isopropanol for 24 h (PDF)

■ AUTHOR INFORMATION

Corresponding Author

*E-mail: christophe.detavernier@ugent.be. Tel: +32-09-2644342. Fax: +32-09-2644996.

ORCID

Bo Zhao: 0000-0002-4452-1735
Felix Mattelaer: 0000-0001-6275-6805
Jolien Dendooven: 0000-0002-2385-3693
Christophe Detavernier: 0000-0001-7653-0858

Notes

The authors declare no competing financial interest.

■ ACKNOWLEDGMENTS

We acknowledge FWO-Vlaanderen (grant numbers 1S68518N and GO87418N) and BOF-UGent (UGent GOA nos. 01G01513 and 01G01019) for financial support. We thank Dr. Christian Dussarrat and Dr. Quentin Demarly from Air Liquide for discussions and for providing us with the $Y(EtCp)_2(iPr\text{-}amd)$ precursor. We also thank Matthias Minjauw for assistance with the XPS measurements and analysis, Olivier Janssens for assistance with the SEM/EDX measurements, and Prof. Dr. Diederik Depla for enabling the water contact-angle measurements.

■ REFERENCES

(1) Mudavakkat, V. H.; Atuchin, V. V.; Kruchinin, V. N.; Kayani, A.; Ramana, C. V. Structure, morphology and optical properties of nanocyrstalline yttrium oxide (Y_2O_3) thin films. *Opt. Mater.* **2012**, *34*, 893−900.

(2) Klein, P. H.; Croft, W. J. Thermal Conductivity, Diffusivity, and Expansion of Y_2O_3, $Y_3Al_5O_{12}$, and LaF_3 in the Range 77°-300 K. *J. Appl. Phys.* **1967**, *38*, 1603−1607.

(3) Andrievskaya, E. R. Phase diagram of the ZrO_2-Y_2O_3-Sm_2O_3 system in the melting-point region. *Powder Metall. Met. Ceram.* **2006**, *45*, 346−352.

(4) Huang, D.; Tian, Z. B.; Cui, W.; Gao, L. Q.; Liu, Z.; Diao, X. G.; Liu, G. H. Effects of Y_2O_3 and yttrium aluminates as sintering additives on the thermal conductivity of AlN ceramic substrates. *Ceram. Int.* **2018**, *44*, 20556−20559.

(5) Fan, W.; Bai, Y.; Wang, Z. Z.; Che, J. W.; Wang, Y.; Tao, W. Z.; Wang, R. J.; Liang, G. Y. Effect of point defects on the thermal conductivity of Sc_2O_3-Y_2O_3 co-stabilized tetragonal ZrO_2 ceramic materials. *J. Eur. Ceram. Soc.* **2019**, *39*, 2389−2396.

(6) Zeng, W.; Liu, Q. J.; Liu, Z. T. Structural, Electronic, and Optical Properties of Cubic Y_2O_3: First-Principles Calculations. *Moscow Univ. Phys. Bull.* **2018**, *73*, 95−100.

(7) Rubio, E. J.; Atuchin, V. V.; Kruchinin, V. N.; Pokrovsky, L. D.; Prosvirin, I. P.; Ramana, C. V. Electronic Structure and Optical Quality of Nanocrystalline Y_2O_3 Film Surfaces and Interfaces on Silicon. *J. Phys. Chem. C* **2014**, *118*, 13644−13651.

(8) Boukerika, A.; Guerbous, L. Annealing effects on structural and luminescence properties of red Eu^{3+}-doped Y_2O_3 nanophosphors prepared by sol-gel method. *J. Lumin.* **2014**, *145*, 148−153.

(9) Khodaei, M.; Yaghobizadeh, O.; Shahraki, A. A.; Esmaeeli, S. Investigation of the effect of Al_2O_3-Y_2O_3-CaO (AYC) additives on sinterability, microstructure and mechanical properties of SiC matrix composites: A review. *Int. J. Refract. Hard Met.* **2019**, *78*, 9−26.

(10) Gaboriaud, R. J.; Pailloux, F.; Guerin, P.; Paumier, F. Yttrium sesquioxide, Y_2O_3, thin films deposited on Si by ion beam sputtering: microstructure and dielectric properties. *Thin Solid Films* **2001**, *400*, 106−110.

(11) Choi, T.; Shin, S.; Kim, Y. S.; Lee, J. Ferroelectric Bi modified $YMnO_3$ thin films grown on Si (001) using Y_2O_3 buffer layer for metal-ferroelectric-insulator-semiconductor structure. *Integr. Ferroelectr.* **2002**, *45*, 23−29.

(12) Choi, J. H.; Lee, J. Y.; Kim, Y. T. Formation of Y_2O_3 interface layer in a $YMnO_3$/Si ferroelectric gate structure. *Appl. Phys. Lett.* **2000**, *77*, 4028−4030.

(13) Volochova, D.; Diko, P.; Antal, V.; Radusovska, M.; Piovarci, S. Influence of Y_2O_3 and CeO_2 additions on growth of YBCO bulk superconductors. *J. Cryst. Growth* **2012**, *356*, 75−80.

(14) Zhang, Z. W.; Shi, Y. H.; Zhai, W.; Dennis, A. R.; Cardwell, D. A. Effect of Pt and CeO_2 on Growth of Y-123/nano-Y_2O_3 Single Grain Superconductors. *IEEE Trans. Appl. Supercond.* **2016**, *27*, 1.

(15) Venkatachalaiah, K. N.; Nagabhushana, H.; Darshan, G. P.; Basavaraj, R. B.; Prasad, B. D.; Sharma, S. C. Structural, morphological and photometric properties of sonochemically synthesized Eu^{3+} doped Y_2O_3 nanophosphor for optoelectronic devices. *Mater. Res. Bull.* **2017**, *94*, 442−455.

(16) Wang, M.; Xu, L.; Chen, G.; Zhao, X. Topological Luminophor Y_2O_3:Eu^{3+}+Ag with High Electroluminescence Performance. *ACS Appl. Mater. Interfaces* **2019**, *11*, 2328−2335.

(17) Tanner, P. A.; Zhou, X. J.; Liu, F. G. Assignment of electronic transitions and electron-phonon coupling of Er^{3+} doped into Y_2O_3. *J. Phys. Chem. A* **2004**, *108*, 11521−11525.

(18) Ju, G. F.; Hu, Y. H.; Chen, L.; Wang, X. J.; Mu, Z. F.; Wu, H. Y.; Kang, F. W. Luminescence properties of Y_2O_3:Bi^{3+}, Ln^{3+} (Ln = Sm, Eu, Dy, Er, Ho) and the sensitization of Ln^{3+} by Bi^{3+}. *J. Lumin.* **2012**, *132*, 1853−1859.

(19) Cabello Guzman, G.; Gonzalez, D.; Caro Diaz, C.; Lillo Arroyo, L.; Valenzuela Melgarejo, F.; Cardenas Trivino, G. C.; Buono Core, G. E.; Chornik, B.; Huentupil, Y. Preliminary evaluation of the up-conversion emission of Y_2O_3:Er-Yb thin films prepared by a solid state photochemical deposition method. *J. Lumin.* **2018**, *204*, 401−409.

(20) Oh, E. O.; Whang, C. M.; Hwang, H. J.; Lee, Y. R.; Lee, J. H.; Son, J. W.; Kim, B. K.; Je, H. J.; Lee, J. H.; Lee, H. W. Thin Film Yttria-Stabilized Zirconia (YSZ) Electrolyte Fabricated by a Novel Chemical Solution Deposition (CSD) Process for Solid Oxide Fuel Cells (SOFCs). *J. Nanoelectron. Optoelectron.* **2012**, *7*, 554−558.

(21) Khan, M. S.; Lee, S. B.; Song, R. H.; Lee, J. W.; Lim, T. H.; Park, S. J. Fundamental mechanisms involved in the degradation of nickel yttria stabilized zirconia (Ni-YSZ) anode during solid oxide fuel cells operation: A review. *Ceram. Int.* **2016**, *42*, 35−48.

(22) Kulkarni, A.; Giddey, S.; Badwal, S. P. S. Yttria-doped ceria anode for carbon-fueled solid oxide fuel cell. *J. Solid State Electrochem.* **2015**, *19*, 325−335.

(23) Fan, Z.; An, J. W.; Iancu, A.; Prinz, F. B. Thickness effects of yttria-doped ceria interlayers on solid oxide fuel cells. *J. Power Sources* **2012**, *218*, 187−191.

(24) Chen, K.; Li, N.; Ai, N.; Cheng, Y.; Rickard, W. D. A.; Jiang, S. P. Polarization-Induced Interface and Sr Segregation of in Situ Assembled $La_{0.6}Sr_{0.4}Co_{0.2}Fe_{0.8}O_{3-\delta}$ Electrodes on Y_2O_3−ZrO_2 Electrolyte of Solid Oxide Fuel Cells. *ACS Appl. Mater. Interfaces* **2016**, *8*, 31729−31737.

(25) Ji, S.; Cho, G. Y.; Yu, W.; Su, P.-C.; Lee, M. H.; Cha, S. W. Plasma-Enhanced Atomic Layer Deposition of Nanoscale Yttria-Stabilized Zirconia Electrolyte for Solid Oxide Fuel Cells with Porous Substrate. *ACS Appl. Mater. Interfaces* **2015**, *7*, 2998−3002.

(26) Wiktorczyk, T.; Bieganski, P.; Serafinczuk, J. Optical properties of nanocrystalline Y_2O_3 thin films grown on quartz substrates by electron beam deposition. *Opt. Mater.* **2016**, *59*, 150−156.

(27) Varhue, W.; Massimo, M.; Carrulli, J.; Baranauskas, V.; Adams, E.; Broitman, E. Deposition of Y_2O_3 by plasma enhanced organometallic chemical vapor deposition using an electron cyclotron resonance source. *J. Vac. Sci. Technol., A* **1993**, *11*, 1870−1874.

(28) Durand, C.; Vallée, C.; Loup, V.; Salicio, O.; Dubourdieu, C.; Blonkowski, S.; Bonvalot, M.; Holliger, P.; Joubert, O. Metal−insulator−metal capacitors using Y_2O_3 dielectric grown by pulsed-injection plasma enhanced metalorganic chemical vapor deposition. *J. Vac. Sci. Technol., A* **2004**, *22*, 655−660.

(29) Detavernier, C.; Dendooven, J.; Pulinthanathu Sree, S.; Ludwig, K. F.; Martens, J. A. Tailoring nanoporous materials by atomic layer deposition. *Chem. Soc. Rev.* **2011**, *40*, 5242−5253.

(30) Cremers, V.; Puurunen, R. L.; Dendooven, J. Conformality in atomic layer deposition: Current status overview of analysis and modelling. *Appl. Phys. Rev.* **2019**, *6*, No. 021302.

(31) Johnson, R. W.; Hultqvist, A.; Bent, S. F. A brief review of atomic layer deposition: from fundamentals to applications. *Mater. Today* **2014**, *17*, 236−246.

(32) Fang, G. Y.; Xu, L. N.; Cao, Y. Q.; Li, A. D. Theoretical design and computational screening of precursors for atomic layer deposition. *Coord. Chem. Rev.* **2016**, *322*, 94−103.

(33) Bernal Ramos, K.; Saly, M. J.; Chabal, Y. J. Precursor design and reaction mechanisms for the atomic layer deposition of metal films. *Coord. Chem. Rev.* **2013**, *257*, 3271−3281.

(34) Niinistö, J.; Putkonen, M.; Niinistö, L. Processing of Y_2O_3 thin films by atomic layer deposition from cyclopentadienyl-type compounds and water as precursors. *Chem. Mater.* **2004**, *16*, 2953−2958.

(35) Cho, G. Y.; Noh, S.; Lee, Y. H.; Ji, S.; Cha, S. W. Study of Y_2O_3 thin film prepared by plasma enhanced atomic layer deposition. *ECS Trans.* **2014**, *64*, 15−21.

(36) Majumder, P.; Jursich, G.; Kueltzo, A.; Takoudis, C. Atomic layer deposition of Y_2O_3 films on silicon using tris (ethylcyclopentadienyl) yttrium precursor and water vapor. *J. Electrochem. Soc.* **2008**, *155*, G152−G158.

(37) Xu, R.; Selvaraj, S. K.; Azimi, N.; Takoudis, C. G. Growth characteristics and properties of yttrium oxide thin films by atomic layer deposition from novel Y $(iPrCp)_3$ precursor and O_3. *ECS Trans.* **2013**, *50*, 107−116.

(38) Putkonen, M.; Sajavaara, T.; Johansson, L. S.; Niinisto, L. Low-temperature ALE deposition of Y_2O_3 thin films from beta-diketonate precursors. *Chem. Vap. Deposition* **2001**, *7*, 44−50.

(39) Mai, L.; Boysen, N.; Subaşı, E.; de los Arcos, T.; Rogalla, D.; Grundmeier, G.; Bock, C.; Lu, H. L.; Devi, A. Water assisted atomic layer deposition of yttrium oxide using tris (N, N′-diisopropyl-2-

dimethylamido-guanidinato) yttrium (iii): process development, film characterization and functional properties. *RSC Adv.* **2018**, *8*, 4987−4994.

(40) de Rouffignac, P.; Park, J. S.; Gordon, R. G. Atomic layer deposition of Y_2O_3 thin films from yttrium tris (N, N '-diisopropylacetamidinate) and Water. *Chem. Mater.* **2005**, *17*, 4808−4814.

(41) Park, I. S.; Chan Jung, Y.; Seong, S.; Ahn, J.; Kang, J.; Noh, W.; Lansalot Matras, C. Atomic layer deposition of Y_2O_3 films using heteroleptic liquid (iPrCp) 2 Y (iPr-amd) precursor. *J. Mater. Chem. C* **2014**, *2*, 9240−9247.

(42) Seppala, S.; Niinisto, J.; Blanquart, T.; Kaipio, M.; Mizohata, K.; Raisanen, J.; Lansalot-Matras, C.; Noh, W.; Ritala, M.; Leskela, M. Heteroleptic Cyclopentadienyl-Amidinate Precursors for Atomic Layer Deposition (ALD) of Y, Pr, Gd, and Dy Oxide Thin Films. *Chem. Mater.* **2016**, *28*, 5440−5449.

(43) Lee, J. S.; Kim, W. H.; Oh, I. K.; Kim, M. K.; Lee, G.; Lee, C. W.; Park, J.; Lansalot-Matras, C.; Noh, W.; Kim, H. Atomic layer deposition of Y_2O_3 and yttrium-doped HfO_2 using a newly synthesized $Y(iPrCp)_2$(N-iPr-amd) precursor for a high permittivity gate dielectric. *Appl. Surf. Sci.* **2014**, *297*, 16−21.

(44) Boinovich, L. B.; Emelyanenko, A. M. Hydrophobic materials and coatings: Principles of design, properties and applications. *Russ. Chem. Rev.* **2008**, *77*, 583−600.

(45) Halake, K.; Bae, S.; Lee, J.; Cho, Y.; Jo, H.; Heo, J.; Park, K.; Kim, H.; Ju, H.; Kim, Y.; Hasani, A.; Pham, T. D.; Choi, J.; Hong, S.; Choi, S.; Lee, J. Strategies for Fabrication of Hydrophobic Porous Materials Based on Polydimethylsiloxane for Oil-Water Separation. *Macromol. Res.* **2019**, *27*, 109−114.

(46) Mullangi, D.; Shalini, S.; Nandi, S.; Choksi, B.; Vaidhyanathan, R. Super-hydrophobic covalent organic frameworks for chemical resistant coatings and hydrophobic paper and textile composites. *J. Mater. Chem. A* **2017**, *5*, 8376−8384.

(47) Feng, X.; Feng, L.; Jin, M.; Zhai, J.; Jiang, L.; Zhu, D. Reversible super-hydrophobicity to super-hydrophilicity transition of aligned ZnO nanorod films. *J. Am. Chem. Soc.* **2004**, *126*, 62−63.

(48) Singh, V. P.; Sandeep, K.; Kushwaha, H. S.; Powar, S.; Vaish, R. Photocatalytic, hydrophobic and antimicrobial characteristics of ZnO nano needle embedded cement composites. *Constr. Build. Mater.* **2018**, *158*, 285−294.

(49) Feng, X.; Zhai, J.; Jiang, L. The fabrication and switchable superhydrophobicity of TiO_2 nanorod films. *Angew. Chem., Int. Ed.* **2005**, *44*, 5115−5118.

(50) Yang, T. Y.; Chang, S. J.; Li, C. C.; Huang, P. H. Selectivity of Hydrophilic and Hydrophobic TiO_2 for Organic-Based Dispersants. *J. Am. Ceram. Soc.* **2017**, *100*, 56−64.

(51) Azimi, G.; Dhiman, R.; Kwon, H. M.; Paxson, A. T.; Varanasi, K. K. Hydrophobicity of rare-earth oxide ceramics. *Nat. Mater.* **2013**, *12*, 315−320.

(52) Oh, I. K.; Kim, K.; Lee, Z.; Ko, K. Y.; Lee, C. W.; Lee, S. J.; Myung, J. M.; Lansalot Matras, C.; Noh, W.; Dussarrat, C.; Kim, H.; Lee, H. B. R. Hydrophobicity of Rare Earth Oxides Grown by Atomic Layer Deposition. *Chem. Mater.* **2015**, *27*, 148−156.

(53) Xie, Q.; Jiang, Y. L.; Detavernier, C.; Deduytsche, D.; Van Meirhaeghe, R. L.; Ru, G. P.; Li, B. Z.; Qu, X. P. Atomic layer deposition of TiO_2 from tetrakis-dimethyl-amido titanium or Ti isopropoxide precursors and H_2O. *J. Appl. Phys.* **2007**, *102*, No. 083521.

(54) Dendooven, J.; Deduytsche, D.; Musschoot, J.; Vanmeirhaeghe, R. L.; Detavernier, C. Conformality of Al_2O_3 and AlN Deposited by Plasma-Enhanced Atomic Layer Deposition. *J. Electrochem. Soc.* **2010**, *157*, G111−G116.

(55) Musschoot, J.; Xie, Q.; Deduytsche, D.; Van den Berghe, S.; Van Meirhaeghe, R. L.; Detavernier, C. Atomic layer deposition of titanium nitride from TDMAT precursor. *Microelectron. Eng.* **2009**, *86*, 72−77.

(56) Zhang, Y.; Wang, H.; Yan, B.; Zhang, Y. W.; Yin, P.; Shen, G. L.; Yu, R. Q. A rapid and efficient strategy for creating super-hydrophobic coatings on various material substrates. *J. Mater. Chem.* **2008**, *18*, 4442−4449.

(57) Takahashi, N.; Watanabe, K.; Taniguchi, T.; Nagashio, K. Atomic layer deposition of Y_2O_3 on h-BN for a stack in graphene FETs. *Nanotechnology* **2015**, *26*, 175708.

(58) Schrader, M. E. Young-dupre revisited. *Langmuir* **1995**, *11*, 3585−3589.

(59) Zhao, J.; Wang, M.; Gleason, K. K. Stabilizing the Wettability of Initiated Chemical Vapor Deposited (iCVD) Polydivinylbenzene Thin Films by Thermal Annealing. *Adv. Mater. Interfaces* **2017**, *4*, 1700270.

(60) Zubkov, T.; Stahl, D.; Thompson, T. L.; Panayotov, D.; Diwald, O.; Yates, J. T. Ultraviolet light-induced hydrophilicity effect on TiO_2 (110) (1 × 1). Dominant role of the photooxidation of adsorbed hydrocarbons causing wetting by water droplets. *J. Phys. Chem. B* **2005**, *109*, 15454−15462.

(61) Lee, J.; Hwang, S.; Cho, D. H.; Hong, J.; Shin, J. H.; Byun, D. RF plasma based selective modification of hydrophilic regions on super hydrophobic surface. *Appl. Surf. Sci.* **2017**, *394*, 543−553.

(62) Van Deynse, A.; Cools, P.; Leys, C.; Morent, R.; De Geyter, N. Influence of ambient conditions on the aging behavior of plasma-treated polyethylene surfaces. *Surf. Coat. Technol.* **2014**, *258*, 359−367.

(63) De Geyter, N.; Morent, R.; Leys, C. Influence of ambient conditions on the ageing behaviour of plasma-treated PET surfaces. *Nucl. Instrum. Methods Phys. Res., Sect. B* **2008**, *266*, 3086−3090.